Ballistic-type field penetration into metals illustrated by high- and low-frequency size-effect measurements in silver

V. F. Gantmakher

Institute of Solid State Physics, Academy of Sciences of the USSR, 142432, Chernogolovka, USSR

J. Lebech and C. K. Bak

Physics Laboratory I, The Technical University of Denmark, DK-2800 Lyngby, Denmark

(Received 30 January 1979)

Radio-frequency size-effect experiments were performed on silver plane-parallel plates at high, 45 GHz, and low, 3 MHz, frequencies. By investigation of size-effect structures we show the influence of frequency on the field distribution inside the metal. When the frequency increases, the splash structure of the field is eliminated because it takes a finite time for an electron to pass the effective region of the trajectory when compared to the time variation of the applied field. Hence only the field between the splash positions remains. The role of different types of trajectories under these conditions are discussed on the basis of Pippard's ineffectiveness concept. The Fermi velocities along the belly orbit ($\vec{B} \parallel [001]$) in silver are extracted from the high-frequency spectra.

I. INTRODUCTION

When an electromagnetic wave of frequency ω is incident upon the surface of a metal, considered to be under anomalous skin-effect conditions in the presence of a magnetic field, the electromagnetic field may in several cases penetrate to distances x comparable to the mean free path l. The magnetic field $\vec{B}$ is assumed to be parallel to the sample surface, and, further, the condition

$$\delta \ll D < l \qquad (1)$$

is supposed to be fulfilled. D is the diameter of the cyclotron orbit and δ is the skin depth. In a number of cases the penetration of the field into the metal is determined mainly by the shape of the individual electron trajectories. The penetration may then be referred to as being of a ballistic type, in contrast to the wider known wave-type penetration. Ballistic penetration may be caused by effective electrons,[1,2] i.e., those moving parallel to the surface in the skin layer, as well as to ineffective ones.[2] In the former case the space distribution of the field is extremely nonuniform, taking the shape of so-called "field splashes." The ballistic penetration based on ineffective electrons is much more wavelike, and in some cases no sharp division between the two types of field penetration can be made.

Although the existence of the splashes can in some cases be deduced by measurements of the impedance of a semi-infinite specimen,[3] experimental investigations of ballistic field penetration are usually made on plane-parallel samples. Using a one-sided excitation of the electromagnetic field in a plane-parallel sample

of thickness d, the scale of the field distribution inside the sample may be altered by changing the dc magnetic field. By means of a suitable experimental technique, the internal field distribution may be displayed at the far side of the sample. As the effect is linear, one may use a two-sided excitation, each of the sample surfaces operating simultaneously as a transmitting and receiving surface.[4,5] Such experiments are generally called "size-effect experiments" especially at low frequencies, i.e., in the MHz range.

At high frequencies, i.e., in the microwave range, size-effect experiments reveal in addition the existence of time-of-flight effects.[6-14] They appear when the time t, it takes an electron to move between two specified points on its ballistic trajectory, is much larger than the period of the high-frequency field ($\tau = $ relaxation time)

$$\tau \gg t \gg 1/\omega \ . \qquad (2)$$

Then t may be the decisive parameter selecting those trajectories which determine the ballistic-type field penetration. This is in contrast to the phenomenon observed at low frequencies, where only the shape and dimension of the trajectory are of importance.

One of the most striking features of the high-frequency experimental results shown in Refs. 7, 9, and 10 and in Ref. 14 is that the size-effect structure appears on both sides of the cutoff field B_e determined by the equality of the extremal diameter D to the thickness d of the sample, whereas at low frequencies all of the size-effect structure was observed above B_e.[4,15] The latter fact was repeatedly checked in a number of experiments on account of its importance for applications of size-effect results in the
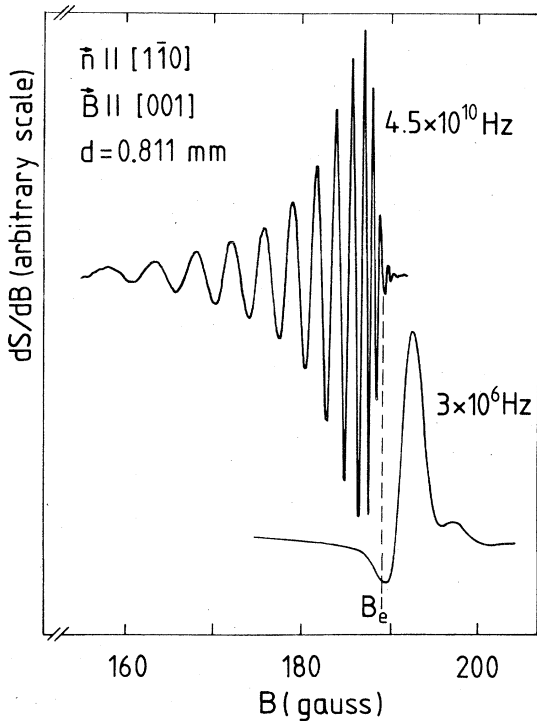
FIG. 1. Derivative of the size-effect signal S with respect to magnetic field B for sample 1 with normal direction $\vec{n}$ and thickness d.

determination of Fermi-surface dimensions. In terms of field penetration, this difference in the size-effect structure as observed at high and low frequencies, respectively, implies that, at high frequencies, regions with nonzero fields are localized, not only immediately adjacent to the planes

$$x = nD \quad (n = 1, 2, 3, ...) \quad , \tag{3}$$

but also in "some vicinity" above these planes. We illustrate this by showing some experimental results (Figs. 1 and 2) which will be described in detail below. In Fig. 1 the high- and low-frequency traces are plotted in the usual coordinates (signals versus applied magnetic field). Figure 2 shows the same data replotted with the axis interchanged so that the vertical axis scales the distance from the surface into the metal and the horizontal axis scales the rf field.

It was this difference that induced us to repeat some of the earlier experiments[7-12] with improved experimental conditions. We thereby hope to clarify the origin of the difference of the field distributions at high and low frequencies. The main changes, relative to the earlier experiments were first, that the sample thicknesses were ~3.5 times larger. Second, that both the high- and the low-frequency experiments were made on the same samples. The high-frequency traces were in addition compared to calcu-
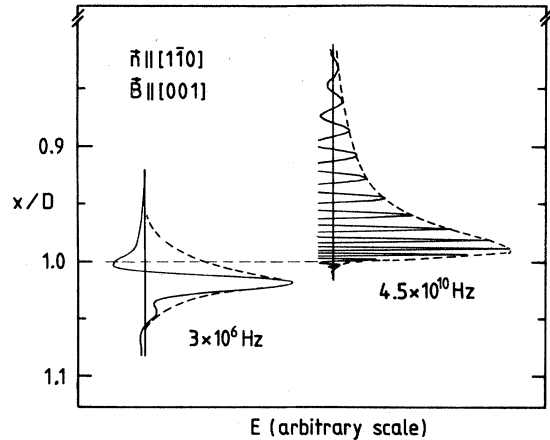

FIG. 2. Envelopes of the experimental traces (sample 1, $\vec{B} \parallel [001]$), illustrating the field penetration at low and high frequencies, E is the magnitude of ac electric field inside the metal.

lations based on the ballistic model.[6,7]

The paper is organized as follows. In Sec. II, we give a qualitative discussion of the ballistic model. This includes a classification of the various types of trajectories, type-I, -II,[6,7] and -III. With this classification in mind, we then try to obtain a qualitative understanding of the field penetration over a wide frequency range.

Further we present in Sec. III a number of experimental details concerning the samples and the equipment used at high- and low-frequency experiments. In particular, the advantages of using thick samples are discussed.

The main experimental results are collected in Sec. IV. They include a comparison between the high- and low-frequency size-effect structures, the high-frequency size-effect traces in multiple fields, and the low-frequency traces obtained without modulation. The latter permit us to compare the magnitudes of the ac field inside and outside the splash layers. As a whole, the material of Sec. IV illustrates and confirms the qualitative picture of the field penetration presented in Sec. II.

Section V presents a comparison between the experimental results and theoretical calculations within the framework of the ballistic model. The calculations lead to an estimate of the Fermi velocities of silver. In addition some features of the electronic spectrum of silver are briefly discussed in Sec. V. Finally, Sec. VI contains a summary and concluding remarks.

II. QUALITATIVE ANALYSIS

A. Classification of trajectories

In this section we define the terminology to be used when examining the experimental results

presented later. We assume that the extremal electron trajectories are of a circular shape along which the electrons move with a constant velocity. Consider next a point A at the depth x from the sample surface, and let $x < D$. The point A may be connected with the sample surface by means of trajectories of different lengths, L, where the L's depend on the angles α at which the electron leaves the surface, i.e., $L = L(\alpha)$. Following[6,7] we refer to the trajectories with starting angle $\alpha = 0$ as type-I trajectories, to the symmetrical ones which intersect the surface and the x level at the same angle as type-II trajectories, and to those which skim the x level as type-III trajectories (see the inset to Fig. 3). One easily finds for the $L(\alpha)$ as respect to D

$$\gamma_{1,2} \equiv 2L(\alpha)/D$$

$$= \pi - \alpha \mp \arccos(2x/D - \cos\alpha) \ . \quad (4)$$

In Fig. 3 we show γ for three different values of x. For each value of x the lower branch of the curve corresponds to the minus sign in Eq. (4). Thus, the lower branch represents trajectories that start at the
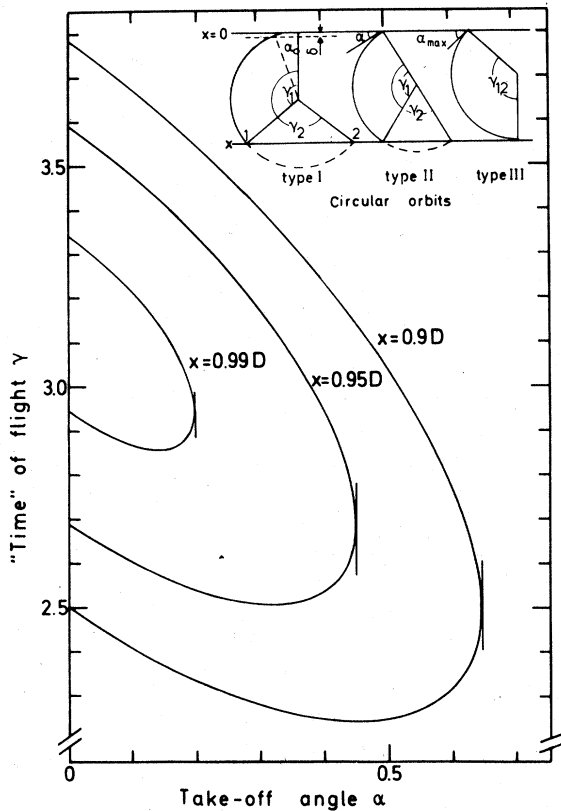
"excitation surface" and pass through x, while the electron is still moving into the metal. Analogously, the upper branch of the curve corresponds to the plus sign in Eq. (4) and represents trajectories in which the electrons pass the x level a second time before returning at the sample surface.

When analyzing the size-effect structure for field values below the cutoff field B_e, the upper branch of the curves in Fig. 3 is of no importance, as the electrons hit the second sample surface at $x = d$, before the velocity component along the sample normal changes sign. It should be noted, that the angle, α, is a convenient variable to use, because the number of electrons leaving the sample surface within an angular spread $d\alpha$ is constant along the α axis of Fig. 3. This would not have been the case if instead L had been expressed as $L = L(X)$ where the variable $X = (D/2)\cos\alpha$ is the depth of the center of the trajectory.

According to the solution of Boltzmann's equation presented by Chambers,[16] the contribution from an electron to the current and field at the point A depends on the values of the field at all points along the electron trajectory. We assume, however, that the electronic motion is seriously influenced only by the field in the skin layer near the sample surface. Then, with the skin layer thin enough the phase of the field contribution from a given electron to the total field at the point A will depend strongly on the L value of the corresponding trajectory. The contributions from the different trajectories will cancel because of interference except for those trajectories which have L values close to the minimum of the function $L(\alpha)$. This follows from the usual principle selecting extremal trajectories from the vicinity of a stationary point. The time of flight, $t \propto L$, is here the parameter which has to be stationary and time of flight thus serves to select the contributing trajectories. It follows from Eq. (4), that the trajectory with minimum L value is one for which $X = \frac{1}{2}x$, i.e., the type-II trajectory.

The L value corresponding to the type-I trajectories for which $\alpha = 0$ (type-I) are not extremal since $d\gamma/d\alpha = -1$. However, $L(\alpha)$ breaks off for $\alpha = 0$, and the destructive interference at the depth x may be incomplete, allowing at least in principle, the observation of type-I contributions in addition to type-II contributions. A somewhat similar case of ballistic field penetration, caused by trajectories belonging to so-called boundary sections, was discussed by Kaner and Falko[17]; in that case, too, no stationary point was present.

Type-II contributions are expected to dominate, since type-I terms are of "higher order." It can be argued, however, that certain circumstances may favor an enhancement of contributions coming from trajectories of type-I. Thus trajectories in the angular interval

FIG. 3. Function γ, defined by Eq. (4), calculated for three different values of the distance x below the sample surface. Inset the three different trajectory types used in the analysis of the size-effect structure.

$$0 < \alpha < \alpha_0 \simeq (\delta/D)^{1/2} \qquad (5)$$

will correspond to effective electrons and therefore, from the standpoint of Pippard's ineffectiveness concept,[18] be relatively more important than other trajectories. For electrons satisfying Eq. (5), the phase difference, due to the difference in the lengths of the trajectories, will be small if

$$\omega(D\delta)^{1/2}/v \ll 1 \qquad (6)$$

is satisfied. Because of this, the type-I trajectories can be enhanced by decreasing the frequency ω and/or orbit diameter D. A slight dependence of δ on both ω and B does not alter this tendency.

The point $\alpha_{\max} = \arccos(2x/D - 1)$, at the right end of the α interval in Fig. 3, represents yet another limiting trajectory, which is inverted relative to a type-I trajectory. This limiting trajectory, which we refer to as a type-III trajectory, starts at the sample surface at an angle equal to $\alpha_{\max}$ and skims the x level. The derivative $d\gamma/d\alpha$ becomes infinite at the point $\alpha = \alpha_{\max}$ and, consequently, the type-III trajectories cannot contribute to the field penetration at high frequencies. Below we return, however, to these trajectories in connection with the discussion of the differences between size effects at low and high frequencies.

B. Penetration along chained trajectories

Up to this point we have assumed that the level x and the excitation surface $x = 0$ were mutually connected via a single trajectory. When $x > D$ this becomes impossible and the two points may then only be connected by means of composite trajectories, made up of a number of arcs of cyclotron orbits for the electrons. In fact, for such values of the magnetic field that

$$(n-1)D < x < nD \quad (n = 1, 2, 3, ...) \qquad (7)$$

composite trajectories made up of at least n arcs of cyclotron orbits are needed. All of them, except one, are dislocated inside the metal and do not intersect the skin layer. So their excitation by the field is not concentrated at a definite level, but smeared over the whole trajectory. We can, however, avoid calculating this excitation by comparing the lengths of all possible chains of arcs connecting x level with the surface.

As an illustration, consider the case $n = 2$, i.e., $D < x < 2D$. It can easily be shown, that among all the possible chains with two links, the shortest possible one consists of two equal type-II trajectories centered at the levels $x/4$ and $3x/4$. With the time of flight $t \propto L$ once more being stationary, the time of flight determines the field penetration along a chain of type-II trajectories. The structure of the size effect observed at the fields $2B_e, 3B_e, ...$, etc., may therefore be expected to have an appearance similar to the

one observed at B_e, except for a change of scale by a factor of $2, 3, ...$, etc.

For the sake of completeness, we remark that for a given field range (7) determined by, e.g., $n = n_0$, composite type-II trajectories with $N > n_0$ arcs of cyclotron orbits will yield an additional contribution to the field penetration. This contribution will, however, be of higher order and may be neglected.

A somewhat more peculiar situation is met if the field penetration is determined by type-I trajectories, i.e., when Eq. (6) is valid in addition to Eqs. (7) and (2). Not only the lower branch breaks off, but also the upper does so for $\alpha = 0$. Both branches have the same derivative at $\alpha = 0$, and their contributions to the field at the level x differ in amplitude by a factor of $\exp[(L_+ - L_-)/l]$. If the difference between the lengths of the two branches $L_+ - L_-$ is small as compared to the mean free path l, the interference between contributions from the branches will determine the field distribution in the range $x < D$ of a semi-infinite medium. The field distribution will be of the form of a standing wave with amplitude dependence

$$A(x) \sim \cos\left(\frac{D\omega}{v_F} \alpha_{\max}\right) ,$$

$$\alpha_{\max} = \arccos\left(\frac{2x}{D} - 1\right) . \qquad (8)$$

In a plane parallel plate such a standing wave cannot reach the opposite side because the surface scattering cuts off the trajectories which belong to the upper branch $L_+(\alpha)$. As a result, the size-effect structure below B_e will not reflect the field distribution in a semi-infinite sample and the size-effect structure around $B = 2B_e$ will not be similar to that around $B = B_e$.

C. Comparison of low- and high-frequency experiments

Type-I and type-III trajectories are "semieffective" trajectories in the sense, that an electron for either of these trajectory types will move parallel to the sample surface at one of the two important levels, 0 — corresponding to the sample surface — or x. However, at these levels the interaction with the field will, in addition, be strongly affected by the time of flight along the effective part of the trajectory if the inequality (6) is violated. As far as the $x = 0$ level is concerned, this gives rise to so-called retardation effects[7,19] closely related to time-of-flight effects in the skin layer.[10,13] For type-III trajectories a violation of the inequality (6) implies that the electron is located around the x level for a time which is long compared to the period $2\pi/\omega$ of the field. In this case interference between the contributions from different electrons following the same single trajectory will yield a

vanishingly small total field independently of contributions caused by other trajectories.

Consider now a metallic semi-infinite medium $x > 0$ situated in a magnetic field B. The value of B determines the cyclotron frequency $\Omega = eB/mc$ and, according to Eqs. (2) and (6), three frequency ranges

$$\omega < \Omega \ , \tag{9}$$

$$\Omega < \omega < \Omega (D/\delta)^{1/2} \ , \tag{10}$$

$$\omega > \Omega (D/\delta)^{1/2} \ . \tag{11}$$

In the low-frequency range (9) the penetrating field is concentrated mainly within some layers, or splashes[2] at positions, x, defined by

$$nD < x < n(D + \delta) \ , \quad (n = 1, 2, 3, ...) \ . \tag{12}$$

The field between the splash positions is relatively small because electrons inside the field carrying chain are ineffective [when they are not in the layers defined by Eq. (12)]. In the intermediate-frequency range (10) the phase of the field distribution becomes x dependent. Furthermore, the type-III character of the trajectory reduces the field inside the layers defined by Eq. (12) according to the arguments given above. As a result, the amplitude of the field inside and outside the splashes (12) may become of the same order of magnitude. Finally, at high frequencies (11) the interference effects reduce the field within the layers so much that the field between the splash positions (12) is now essentially the only field in the bulk sample. In the related size-effect phenomena the B value is determined by the specimen thickness, $B \sim B_e$, and this defines the frequency scale in Eqs. (9) to (11).

Another difference between the field pattern at high and low frequencies should be kept in mind. This concerns the direction of the electric field vector. At low frequencies, the normal component, i.e., the x component, of the electric field will be very small because the contributions from the points 1 and 2 of each of the trajectories (see Fig. 3) are of opposite sign and cancel each other. However, at high frequencies these contributions have different phases and do not, in general, cancel each other. Therefore the electric field inside metal contains an x component at high frequencies.

III. EXPERIMENTAL

A. Samples

In the experiments two samples with normal directions and thicknesses as follows were used: sample 1, $\langle 110 \rangle$ and 0.811 mm, and sample 2, $\langle 100 \rangle$ and 0.870 mm. The samples were prepared by Gasparov, who used them in his measurements on electron-phonon scattering.[20] According to the results described in Ref. 20 the residual resistivity ratio is approximately 1.6×10^4. In the present experiments we used samples which were ~ 3.5 times thicker than the one used earlier, thicker, not only on an absolute scale, but also relative to the mean free path of the electrons. This is an advantage in at least three respects. First, the time-of-flight effects should be more pronounced because the electronic path from one side of the sample to the other is increased. Second, the use of a thick sample ensures that effects caused by many revolutions of the electron in its cyclotron orbit are avoided. This is of importance for fields $B > B_e$. It follows because even the probability of an electron to complete one revolution and thus return to the entrance side of the sample without being scattered is rather small. Certainly, the probability that an electron which leaves one side of the sample will reach the other side of the sample in one half of a revolution without being scattered, is also smaller than unity. This leads of course to a decreased signal level which is compensated by the high sensitivity of the spectrometer used. Third, as the probability of scattering is much larger near the neck regions of the Fermi surface,[20] one deals essentially only with cyclotron orbits on the central belly cross section of the Fermi surface, sufficiently far away from the neck regions; and other extremal cross sections in the present experiments did not give rise to interference effect in the transmitted signal.

B. High-frequency spectrometer

The present high-frequency experiments were performed at 45 GHz, by means of a conventional microwave spectrometer. The spectrometer is the same as the one used in the earlier experiments[6-14] on related problems. In the present experiments the spectrometer was operated in a transmission configuration with the sample forming a part of the common end wall between the input and output cavity. The sample was attached to the cavities, which were made of silver, by means of a conductive silver glue. The experiments were performed at 4.2 K, and a low-pressure exchange gas in the brass can surrounding the cavity system secured the thermal contact to the liquid-helium bath. It was verified experimentally that a 10 dB increase of the microwave power level had no influence on the position of the observed oscillations.

The magnetic field, parallel to the sample surface, was produced by means of a superconducting magnet. Within an angular range of $\sim 5°$ the field direction could be rotated in the sample surface and tipped relative to the sample surface. The zero of the magnetic field axis was carefully determined by observing the position of the relevant signal for opposite field directions, produced by changing the current direction in the solenoid.

C. Low-frequency bridge

The low-frequency experiments were performed at 3 MHz, where the specimen was placed in a coil. The coil impedance was measured by means of a bridge circuit, which will be described in detail elsewhere.[21] The reactance was balanced by switching fixed capacitors forming a binary sequence and the final adjustment was made via the frequency vernier of a highly stable generator system, thus avoiding variable capacitors. Similarly, the resistance was balanced by means of fixed metal film resistors and a continuously variable resistor. The bridge circuit and a preamplifier form an integral part of the Dewar top-flange in order to minimize the cable lengths. The coil containing the sample and the bridge were designed to noise match the input of the preamplifier, resulting in a noise output determined by thermal noise in the loss balancing resistors. The amplifier output and a reference signal were applied to a balanced mixer, producing a dc voltage. This method has two advantages: (a) Either the reactive or the resistive part of the impedance can be measured, depending on the phase adjustment of the reference signal; and (b) the noise bandwidth of the system is determined by the equipment following the mixer. This equipment could be a dc recorder or, in case the derivative with respect to the magnetic field was measured, a phase-sensitive detector.

IV. EXPERIMENTAL RESULTS

Typical examples of experimental traces are shown in Figs. 4(a) and 4(b). The cutoff fields B_e are known from the Fermi-surface dimensions[22] and the sample thickness with an accuracy of at least 0.3%.[20]

These traces differ from those obtained[6-14] with a thinner sample in two aspects. First, the appearance of the traces is typical for type-II contributions only (cf. the analysis of the trace shapes in Ref. 7). Although we have examined many different combinations of directions $(\vec{n}, B)$, none of the observed size-effect structures could be attributed to type-I trajectories. Even for $\vec{B} \parallel [110]$ and $\vec{n} \parallel [1\bar{1}0]$, a case where the central open orbit does not contribute to the size effect, the present observations only show a weak type-II structure apparently belonging to a noncentral cross section. No signal was observed in the low-field region $B < 0.8B_e$, where clear type-I signals were observed in Refs. 6, 7, and 11.

Second, the type-II size-effect structures, observed previously,[6-10] included signals above and below B_e, approximately of the same order of magnitude. In contrast, it may be stated that the signals observed in the present high-frequency experiments immediately above the cutoff field B_e are at least ten times weaker than the signals observed below B_e.

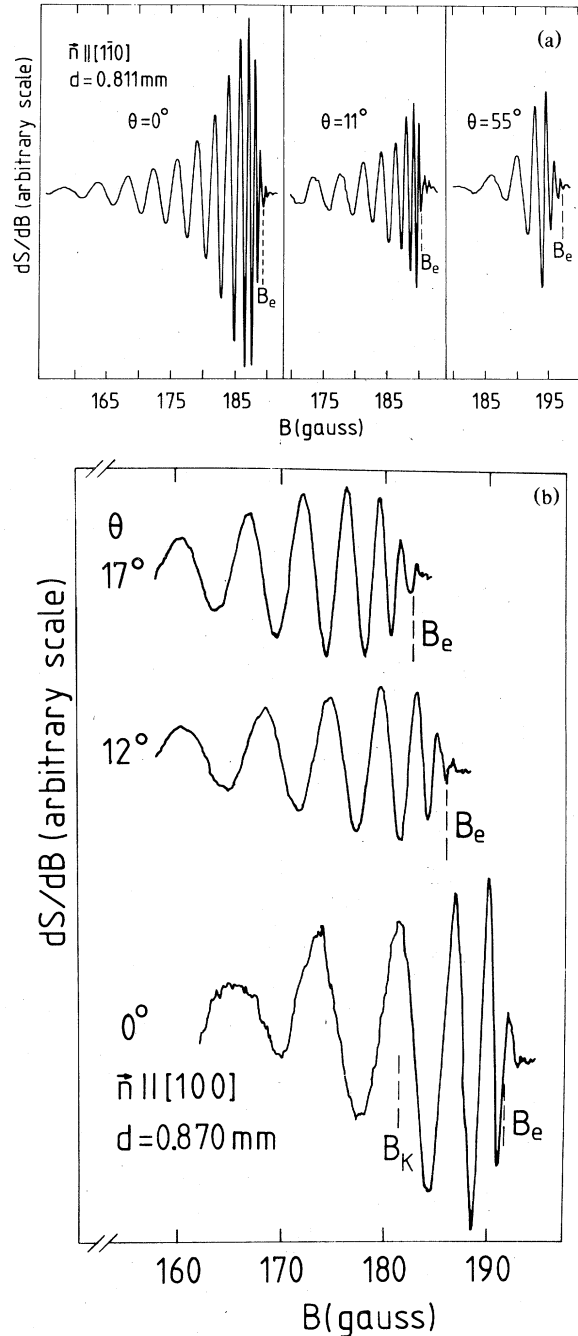Figure 1, showing a high-frequency trace and the

FIG. 4. Experimental size-effect traces in silver at 45 GHz. The angles θ specify the direction of the magnetic field B, relative to the [001] direction. B is parallel to the surface plane. (a) sample 1: $\vec{n} \parallel [1\bar{1}0]$, $d = 0.811$ mm (b) samples 2: $\vec{n} \parallel [100]$, $d = 0.870$ mm. For a definition of B_k see text and Fig. 9.

corresponding low-frequency one clearly demonstrates the difference in size-effect structures, which was discussed in qualitative terms in Sec. II. The experimental plots obviously belong to the two extreme

frequency ranges defined by Eqs. (9) and (11). The plots in Refs. 6 to 10 showing size-effect structure above and below B_e of comparable magnitude, apparently represent the intermediate-frequency range (10). This may result from the use of a thinner sample, because the d value affects Ω as well as D in Eqs. (10) and (11). The fact that the experimental conditions in Refs. 6–14 correspond to Eq. (10) was confirmed by the existence of type-I signals in the experimental results of Refs. 6–14.

As the size-effect structure reflects the field distribution in a semi-infinite medium, the envelopes of the traces may be considered as an indicator of these distributions in the high- and the low-frequency limits, although disturbance caused by the modulation must be kept in mind. The high-frequency signal in essence reveals the field distribution that exists between the splashes at low frequency although it is too small to be observed when compared to the splash field.

In order to obtain an estimate of the ratio of the field outside to the field inside splash layers from the experiment, we have made low-frequency measurements without modulation. The sample is placed inside a coil (Sec. III) and the observed signal is a mixture of a reflected and transmitted signal. The first of these signals is supposed to vary rather smoothly with B, probably affected mainly by the change in magnetoresistance. We therefore set the phase of the bridge circuit at a value which made the slowly varying background signal as weak as possible. A result of such a measurement is shown in Fig. 5. The dotted line indicates the remaining background signal, and the difference between this line and the full line is supposed to be a measure of the transmitted signal and thus, approximately, to represent the field distribution.

As it is seen from Fig. 5, the field outside the splashes amounts to no more than $\sim 5\%$ of the field inside the splash region, at least for the first 3 to 4 splashes. When the frequency increases, however, and the interference effects eliminate the field inside the layers (12), this "5%" is the only field which remains inside the metal and which experimentally may be seen in the plots in Figs. 2 and 3. In Figs. 2 and 3 the signals are enhanced by the use of a standard modulation technique, which could be used because the phase of the signal now depends on x or, equivalently, on B. It should be noted, however, that even at high frequencies it was possible to observe the directly transmitted, unmodulated signal.

The size-effect structure in the vicinity of the field values $2B_e$, $3B_e$,.... is shown in Fig. 6. As stated in Sec. II, the size-effect line structure at the fundamental edge is reproduced at the higher edges, except of a change of scale in the magnetic field values, but it must be emphasized that this is true only for the
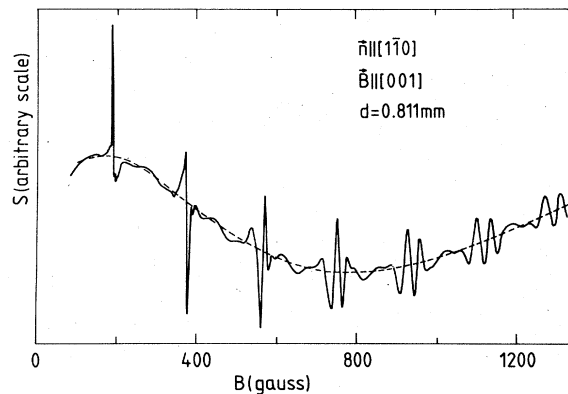

FIG. 5. Size-effect structure in silver observed at the first seven size-effect edges at 3 MHz. Sample 1, $\vec{B} \parallel [001]$. No magnetic field modulation was applied. As explained in the text, the difference between the solid and dotted curves is supposed to represent the transmitted signal.
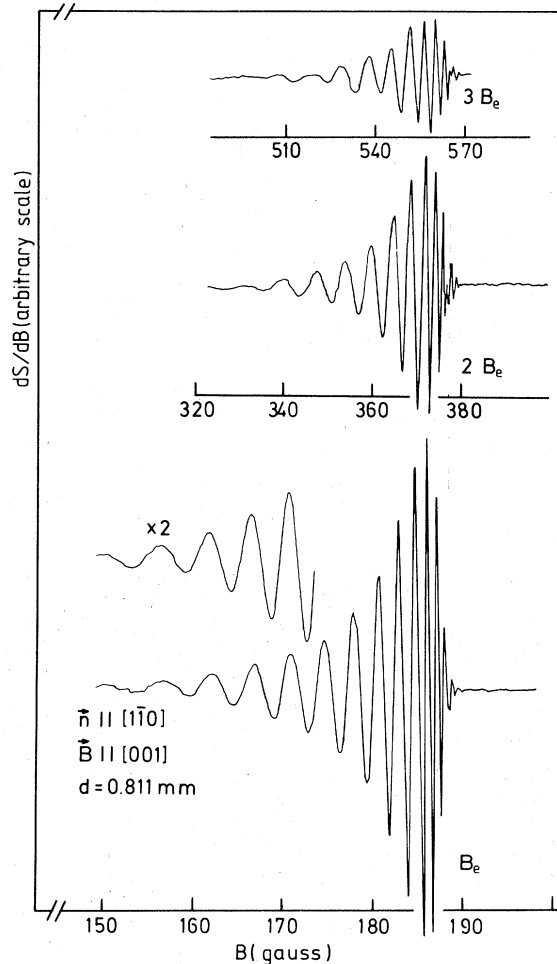

FIG. 6. Size-effect structure in silver observed at the first three size-effect edges at 45 GHz. Sample 1, $\vec{B} \parallel [001]$.

type-II structure. It is also worth noting that ballistic field penetration caused by type-I trajectories is, as of yet, not investigated experimentally in sufficient details. Further experiments, especially at frequencies of the order of ~10 GHz on thick samples, may clarify the role of the type-I trajectories.

V. CALCULATIONS WITHIN THE BALLISTIC MODEL

The calculations to be presented in this section follow closely the lines given in Ref. 7. The calculations are only valid in the high-frequency regime, and only magnetic fields below B_e are considered. The theoretical model applies simplifying assumptions, the most important being: (i) The electric field distribution is not calculated self-consistently, but is described by

$$E(x) \sim e^{-x/\delta} \; , \tag{13}$$

where the complex skin depth

$$\delta = \delta_r + i \delta_i = \delta_0 e^{i \pi / 6} \; ;$$

and the field is supposed to be parallel to the sample surface. (ii) Integration over the entire Fermi surface is abandoned and only one stationary orbit is taken into account, i.e., the central cross section of the silver Fermi surface. (iii) The only trajectories within this cross section that are left are those in the vicinity of the stationary point, i.e., the type-II trajectory.

These assumptions mean that the calculations remain within the frame of the ballistic model. As compared to the qualitative analysis of the Sec. II they involve finite skin depth (13) and may take into account the true shape of the Fermi surface.

A theoretical type-II spectrum for $\bar{n} \parallel [110]$ and $\bar{B} \parallel [001]$ is shown in Fig. 7. The parameters are chosen to match the experimental situation of the
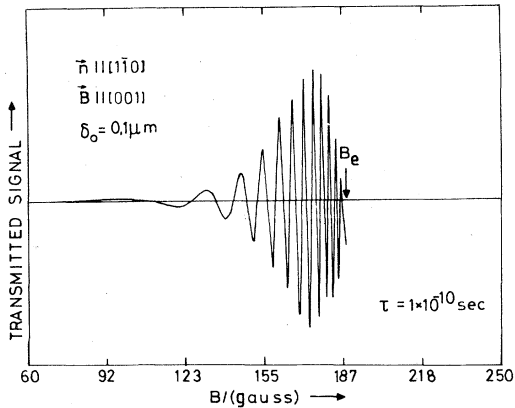

FIG. 7. Calculated type-II transmission spectrum (field modulated) for the central (001) belly orbit. $\bar{B} \parallel [001]$, $\bar{n} \parallel [1\bar{1}0]$.

data shown in Fig. 1 in the high-frequency region (45 GHz). The Fermi velocities and Fermi-surface dimensions are derived from the Fourier models "Ag $5^{\pm}$" by Halse.[22] "Ag 5" denotes Halse's Fourier model of the Fermi surface for silver including the first 5 terms and $\pm$ indicates a numerical differentiation yielding Fermi velocities. The qualitative similarity between the calculated spectrum and the experiment is evident. However, the question arises to what extent the field penetration can be considered within the framework of the ballistic model and for which parameters other phenomena start to be important. These other phenomena may be classified as "collective phenomena"; they appear as field penetration related to an excitation of the electron system as a whole.

To answer this question we tried to extract Fermi velocities from the high-frequency spectra starting at the known Fermi-surface shape and from the ballistic model calculations and we further tried to estimate to what extent the results would be self-consistent.

The procedure of extracting the Fermi velocities from an experimental trace is given in Ref. 7. By differentiating the dependence of B on the time of flight along the type-II trajectory

$$t(b) = \frac{2 \hbar c}{eB} \int_0^{k_y} \frac{dk}{v_x} \; , \quad k_y = \frac{eBD}{2 \hbar c} \; , \tag{14}$$

one obtains

$$v_x = \frac{\omega D}{B(d\phi/dB) + \phi} \; , \quad \phi = \omega t \; . \tag{15}$$

From the experimental trace we deduce only the change of phase $\Delta \phi(B)$ but $\phi(B_e) = \pi B_c / B_e$ is known from the cyclotron mass $(B_c = \omega mc/e)$. So

$$\phi = \Delta \phi(B) - \Delta \phi(B_e) + \pi B_c / B_e \tag{16}$$

and we get $v_x(K_y)$ from Eqs. (14) and (16) and, using a proper Fermi-surface model,[22] the full group velocity v as a function of position on the orbit.

The actual calculations are, however, complicated by the fact that the experiment does not give the transmission $S = S_0 \cos \phi$ directly, but its derivative

$$\frac{dS}{dB} \equiv T = T_0 \cos(\phi - \phi_1) \; . \tag{17}$$

Therefore, in order to obtain the phase function (16) for S from $\phi - \phi_1$ at T, it is necessary to correct for the B-dependent amplitude factors. As ϕ_1 is small, it can be taken in a form

$$\tan \phi_1 \simeq \frac{1}{T_0} \frac{dT_0}{dB} \left| \frac{d(\phi - \phi_1)}{dB} \right|^{-1} , \tag{18}$$

with all the functions obtained from the B-modulated trace.

Further, for B values near the edge it is important

to include corrections that account for the time of flight within the skin layers. This latter type of correction may be referred to as a retardation correction. It may be expressed as

$$\phi_2 = -2 \arctan \frac{\omega \delta_r - \delta_i/\tau}{v_x - \delta_r/\tau - \omega \delta_i} \; . \tag{19}$$

If one lets $\tau \to \infty$ and $\delta_i \to 0$ in Eq. (19), then $-\phi_2$ expresses the time of flight of the electron through the skin layer δ_r, where the factor of 2 takes into account both surfaces of the plate. As v_x enters in Eq. (19), the actual extraction of the velocities from the experimental data requires self-consistent calculations, where all the corrections in each "loop" are calculated from the velocities deduced in the preceding loop.

In Fig. 8 we show the component of the Fermi velocity normal to the sample surface as derived from the experimental data shown in Fig. 2. The dashed curve is obtained from the raw data after a smoothing, whereas the full-line curve shows the velocities after applying the above-mentioned corrections. It appears that substantial errors may result if the corrections (18) and (19) are omitted.

An estimate of the accuracy of the calculated velocities is difficult because the effect of the simplifying assumptions is unknown. A check of the estimate, however, can be made by calculating the velocity from the results of another experiment with the same field direction $\vec{B} \parallel [001]$, but with the normal $\vec{n} \parallel [100]$. In this case the signal is much weaker because the orbit enters the skin layer at a corner and not at its flat part. Furthermore, the orbit size varies rather rapidly so the region of similar orbits near the stationary orbit is narrow. Nevertheless, the trace
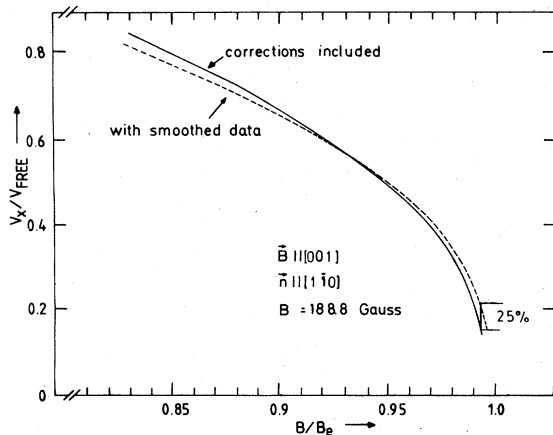
can be worked out in the same manner. The result is shown in Fig. 9.

A pronounced link is observed in the curve at $B = B_k$. This is not compatible with a model assuming that the entire spectrum is caused by type-II contributions from the region near the stationary orbit on the Fermi surface. We assume that the part of the spectrum above B_k is due to type-II central belly contributions only. The spectrum for $B < B_k$ has other contributions also, apparently, from the type-II trajectories of the noncentral orbits.

It is straightforward[7] to arrive at the Fermi velocities around the orbit considered from the deduced normal velocities as a function of B. This is done by using a good Fermi-surface model,[20,22] and yield Fermi-surface dimensions. The result of such a calculation is given in Fig. 10 along with other experimental data available. The first, and most important point to note is that the "experimental" velocities were derived from two experiments corresponding to overlapping angular ranges. The circles (Fig. 10) refer to the experiment for $\vec{n} \parallel [1\bar{1}0]$, and the triangles to the case of $\vec{n} \parallel [100]$ (the range $B_k < B < B_e$ only).

The high-field regime of the latter experiment corresponds to the low-field range of the former. In other words, the electrons which are nearly effective in the case of $\vec{n} \parallel [100]$ are ineffective in the case of $\vec{n} \parallel [1\bar{1}0]$ and vice versa. In spite of these differences, we see that the velocities derived from the two sets of experimental data gree within the error (2%) in the overlap regime. We may therefore conclude
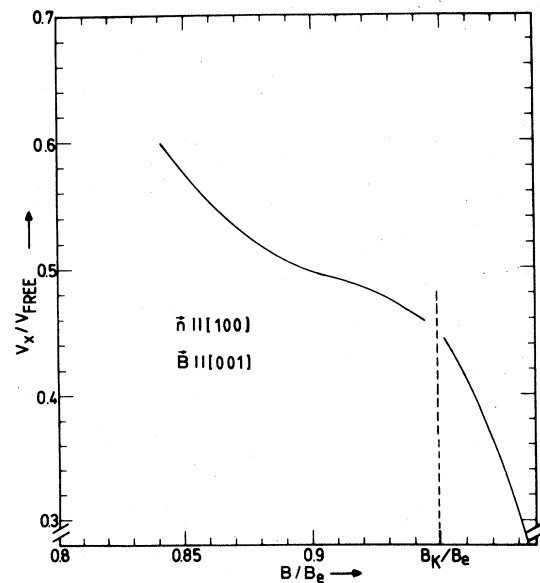

FIG. 8. Transverse velocity v_x as a function of B for the central (001) belly orbit derived from the experiments with $\vec{n} \parallel [1\bar{1}0]$ and $\vec{B} \parallel [001]$. The dashed curve gives v_x calculated directly from the smoothed phase function obtained from the experiment, whereas the curve shown with a solid line includes all the corrections described in the text.

FIG. 9. Transverse velocity v_x (including corrections) derived from the experiment where $\vec{n} \parallel [100]$ and $\vec{B} \parallel [001]$. The part of the curve above $B = B_k$ is assumed to correspond to type-II signals from the central belly orbit.
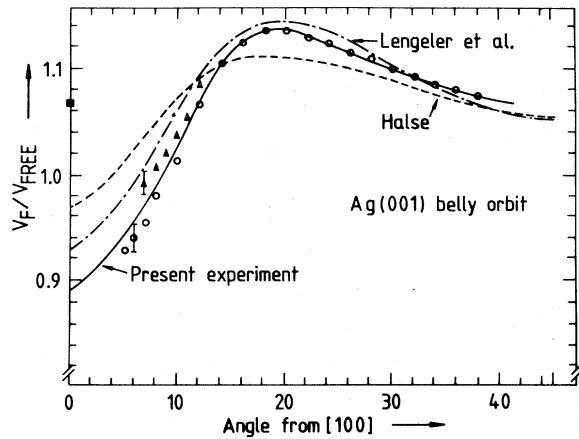
FIG. 10. Velocities derived from the experimental transverse velocities; Fig. 8 (circles) and Fig. 9 (triangles). The curve shown with a solid line represents a least-squares fit to the experiments. The error bars indicate the estimated experimental uncertainty (~2%). The dashed curve represents the velocity derived from Halse's (Ref. 22) Fourier models Ag $5^{\pm}$ which essentially are fitted to Howard's (Ref. 23) cyclotron mass data. The dash-dotted curve represents data obtained by Lengeler *et al.* from de Haas–van Alphen measurements (Ref. 24). The filled square is the velocity value from Ref. 25.

that within accuracy of the present experiment, the small B/B_e value does not itself restrict the applicability of the ballistic model.

In Fig. 10, we have also shown (dashed curve) the velocities derived from Halse's "Ag 5^{+}" and "Ag 5^{-}" Fourier models[22] which essentially are fits to the cyclotron experiment by Howard.[23] It appears that the experimental velocities as derived in the present work differ slightly from those given by Halse. However, they agree well with the data obtained recently by Lengeler *et al.*[24] from de Haas–van Alphen measurements. The filled squre is the velocity value from Ref. 25.

VI. CONCLUSIONS

The qualitative approach based upon an examination of the shape of the trajectories of the charge carriers has once more proved itself to be a powerful tool, though this time it was applied to ineffective electrons which leave the surface at an angle $\alpha \neq 0$. This approach allowed us to set up a universal picture of the field penetration for a wide frequency range. The relations between the period of the electromagnetic field $1/\omega$ and the time it takes an electron to pass the whole trajectory $1/\Omega$ or its part in the skin layer $\delta^{1/2}/D^{1/2}\Omega$ separate the frequency regime into three subbands (9)–(11). It seems, that the three different kinds of experiments which were at our disposal: the high-frequency ones with thin and thick samples, respectively, and the low-frequency experiment on the thick samples, correspond to different subbands. In the lower subband (9) the field is concentrated mainly inside the splash layers and the field outside the splashes does not exceed ~5% of the field in the splash layer. In the upper subband (11) the long time of flight through the vicinity of the effective point of the trajectory eliminates the splash field completely, causing the field between the splash positions to be dominant. Though this field is carried along inside the metal by ineffective type-II trajectories, we did not observe any signs of collective phenomena which could not be included in the ballistic model.

[1]M. Ya. Azbel', Zh. Eksp. Teor. Fiz. **39**, 400 (1960) [Sov. Phys. JETP **12**, 283 (1961)].

[2]E. A. Kaner and V. F. Gantmakher, Usp. Fiz. Nauk. **94**, 193 (1968) [Sov. Phys. Usp. **11**, 81 (1968)].

[3]C. C. Grimes, A. F. Kip, F. N. Spong, R. A. Stradling, and P. Pincus, Phys. Rev. Lett. **11**, 455 (1963).

[4]V. F. Gantmakher, in *Progress in Low Temperature Physics,* edited by C. J. Gorter (North-Holland, Amsterdam, 1967), Vol. 5, p. 181.

[5]W. M. Walsh, Jr., in *Solid State Physics,* edited by J. F. Cochran and R. R. Haering (Gordon and Breach, New York, 1968), Vol. I.

[6]J. O. Henningsen and D. S. Falk, Phys. Rev. Lett. **26**, 1174 (1971).

[7]D. S. Falk, J. O. Henningsen, H. L. Skriver, and N. E. Christensen, Phys. Rev. B **6**, 377 (1972).

[8]J. Lebech and K. Saermark, Phys. Lett. A **36**, 269 (1971).

[9]K. Saermark and J. Lebech, Phys. Lett. A **38**, 121 (1972).

[10]K. Saermark and J. Lebech, Phys. Lett. A **39**, 209 (1972).

[11]S. Brock, thesis (Techn. Univ. Denmark, Lyngby, 1974) (unpublished).

[12]K. Saermark and J. Lebech, Phys. Lett. A **59**, 145 (1976).

[13]M. Surma, J. Lebech and K. Saermark, in *Proceedings of the 14th International Conference on Low Temperature Physics, Helsinki, 1975,* edited by M. Krusius and M. Vuorio (North-Holland, Amsterdam, 1975), p. 329.

[14]J. Lebech and K. Saermark, (unpublished). This paper deals with size effect for $\bar{\text{B}}$ ∥ ⟨111⟩ in a (011) plane.

[15]J. F. Koch and T. K. Wagner, Phys. Rev. 151, 467 (1966).

[16]R. G. Chambers, Proc. Phys. Soc. London Sect. A 65, 458 (1952).

[17]E. A. Kaner and V. L. Valko, Zh. Eksp. Teor. Fiz. 49, 1895 (1965).

[18]A. B. Pippard, Rep. Progr. Phys. 23, 176 (1960).

[19]H. D. Drew, Phys. Rev. B 5, 360 (1972).

[20]V. A. Gasparov, Zh. Eksp. Teor. Fiz. 68, 2259 (1975) [Sov. Phys. JETP 41, 1129 (1976)].

[21]C. K. Bak (unpublished).

[22]M. R. Halse, Philos. Trans. R. Soc. London 265, 507 (1969).

[23]D. G. Howard, Phys. Rev. 140, 1705 (1965).

[24]B. Lengeler et al., Phys. Rev. B 15, 5493 (1977).

[25]P. Deimel and R. E. Doezema, Phys. Rev. B 10, 4897 (1974).